Journal of Power Sources 482 (2021) 228909

Contents lists available at ScienceDirect

Journal of Power Sources

journal homepage: www.elsevier.com/locate/jpowsour

Cobalt substituted $Pr_2Ni_{1-x}Co_xO_{4+\delta}$ ($x = 0$, 0.1, 0.2) oxygen electrodes: Impact on electrochemical performance and durability of solid oxide electrolysis cells

V. Vibhu [a,*], I.C. Vinke [a], R.-A. Eichel [a,b], L.G.J. de Haart [a]

[a] Institute of Energy and Climate Research, Fundamental Electrochemistry (IEK-9), Forschungszentrum Jülich GmbH, 52425, Jülich, Germany
[b] Institute of Physical Chemistry, RWTH Aachen University, 52074, Aachen, Germany

HIGHLIGHTS

- $Pr_2Ni_{1-x}Co_xO_{4+\delta}$ nickelates as O_2-electrode materials for SOEC is reported first time.
- An increase in oxygen content is observed with increasing cobalt content.
- $Pr_2Ni_{0.8}Co_{0.2}O_{4+\delta}$ electrode containing single cell shows the best cell performance.
- Lowest degradation is observed for $Pr_2Ni_{0.8}Co_{0.2}O_{4+\delta}$ electrode under SOEC operation.

GRAPHICAL ABSTRACT

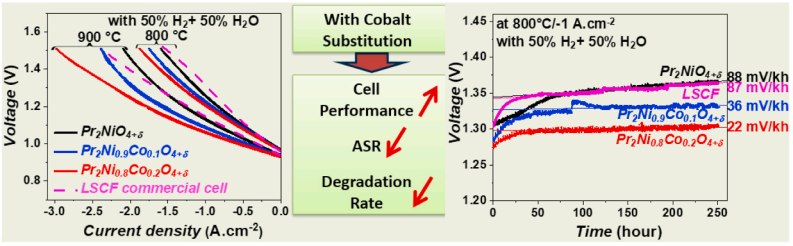

ARTICLE INFO

Keywords:
Nickelates
Solid oxide electrolysis cells (SOECs)
Oxygen over-stoichiometry
Electrochemical performance
Distribution of relaxation times (DRT)
Degradation

ABSTRACT

This study is focused on the development of layered perovskites based alternative oxygen electrodes for high temperature Solid Oxide Electrolysis Cells (SOECs). In this respect, rare earth nickelates $Ln_2NiO_{4+\delta}$ (Ln = La, Pr or Nd) have taken considerable attention due to their good electrochemical properties resulting from high oxide ion diffusivity and a large surface exchange rate. Among them, $Pr_2NiO_{4+\delta}$ (PNO) shows the best electrochemical properties, however, it displays relatively higher degradation rate under SOEC operation at high current density. Therefore, in this work, we perform further modification by substituting nickel by cobalt in order to enhance the physico-chemical properties, electrochemical performance and most importantly the durability of SOECs. Three compositions ($x = 0.0$, 0.1 and 0.2) are prepared and characterized using different techniques. The electrochemical measurements are performed with symmetrical as well as single cells using DC- and AC-techniques in the 700–900 °C temperature range. The electrode reaction mechanism is also examined by recording the impedance spectra at different pO_2. An improvement in electrochemical performance as well as lower degradation rate is observed with cobalt substitution, during short term SOEC operation at -1 A·cm^{-2} current density at 800 °C with 50% H_2 and 50% H_2O feed gas mixture.

1. Introduction

The need of renewable and clean energy sources such as solar, wind, tidal or hydro energy has been growing significantly during last decade. However, due to intermittent nature and location constraint of renewable energy sources, a large-scale electricity storage is needed in order to

* Corresponding author.
E-mail address: v.vibhu@fz-juelich.de (V. Vibhu).

https://doi.org/10.1016/j.jpowsour.2020.228909
Received 21 July 2020; Received in revised form 24 August 2020; Accepted 7 September 2020
Available online 17 September 2020

secure a continuous energy supply. The renewable energy sources can be used to produce hydrogen from water by electrolysis [1,2]. The steam electrolysis using solid oxide electrolysis cells (SOECs) is anticipated to consume less electrical energy for the reaction as compared to electrolysis at low temperature as consequence of the more favourable thermodynamic and electrochemical kinetic conditions. In addition, for high temperature SOECs the high cost noble metal catalysts can be replaced with low cost materials with high electrochemical performance. The high temperature SOEC is not only used for steam electrolysis but also capable of CO_2 electrolysis and co-electrolysis of CO_2–H_2O with the aim to produce syngas [3–6].

One of the essential aspects to achieve the highly efficient SOECs is to enhance the performance and durability of oxygen electrodes, which is limited due to their large degradation during long term under operating conditions. In this respect, several mixed ionic and electronic conducting (MIEC) oxide materials, without alkaline earth metals *e.g.* Sr or Ba (as they segregate to form less conducting or insulating phases), have been extensively studied during past few years [7–15]. Recently, lanthanide nickelates $Ln_2NiO_{4+\delta}$ (Ln = La, Pr or Nd) [15–18] have gained considerable interest as an alternative to conventional cobaltite-, ferrite- or manganite-based oxygen electrode materials. These nickelate compounds with the K_2NiF_4-type layered structure are favourable due to their high anionic bulk diffusion (D^*) as well as surface exchange coefficients (k^*), good electrical conductivity and thermal expansion properties matching with the other cell components like electrolyte, interconnects *etc.* [19–21]. The structure of these $Ln_2NiO_{4+\delta}$ consists of alternate NiO_2 square plane layers and Ln_2O_2 rock salt layers with a network of interstitial oxygen sites in rock salt layers, leading to the first member ($n = 1$) of the Ruddlesden-Popper series $Ln_{n+1}Ni_nO_{3n+1}$. This type of structure has a strong ability to accept interstitial oxygen located in the Ln_2O_2 rock-salt interlayer leading to a mixed valence of Ni (Ni^{2+}/Ni^{3+}), results in a mixed ionic and electronic conductivity (O^{2-}/e^-) [22,23].

Among the nickelates family, $La_2NiO_{4+\delta}$ (LNO) and $Pr_2NiO_{4+\delta}$ (PNO) are the most studied materials for Solid Oxide Cells (SOCs) application. The amount of interstitial oxygen *i.e.* the δ value in these nickelates is highly dependent on the rare-earth cation size. For instance, $Pr_2NiO_{4+\delta}$ (PNO) shows a large amount of interstitial oxygen ($\delta \sim 0.25$) compared to $La_2NiO_{4+\delta}$ (LNO) ($\delta \sim 0.16$) [9], resulting from the smaller ionic radius of Pr^{3+} (1.126 Å) than La^{3+} (1.16 Å) [24]. PNO shows better transport properties for conductivity (both ionic and electronic), oxygen diffusivity, surface exchange as well as higher electrochemical activities than LNO [9]. In addition, the electrochemical performance of PNO is higher than that of LNO *i.e.* PNO shows lower polarization resistance (R_p) value than LNO. Recently, the long term degradation test of $La_{2-x}Pr_xNiO_{4+\delta}$ ($x = 0$, 0.5 and 2) electrodes using symmetrical half-cells was reported up to 1800 h under ± 300 mA·cm^{-2} current load at 700 °C [25], and concluded that these electrode exhibits almost negligible degradation under SOEC operation compared to the SOFC operation. However, their behaviour under real SOEC conditions using single cells is still not available in the literature. Consequently, an attempt was then made to investigate the electrochemical properties of PNO for use as an oxygen electrode material of SOECs. Later on, further modification was carried out by substitution of cobalt at nickel site, in order to further improve the transport and electrochemical properties of PNO.

Therefore, the present work is focused on cobalt substituted praseodymium nickelates $Pr_2Ni_{1-x}Co_xO_{4+\delta}$ ($x = 0.0$, 0.1 and 0.2) (PNCO) and aims particularly at the enhancement of electrochemical activity and durability of PNO used as oxygen electrode in SOECs. At first, the preliminary structural and physicochemical characterizations are studied. Further the electrochemical activities and reaction mechanism of these materials are investigated with symmetrical half-cells. Finally, the electrochemical performance and short-term durability test under SOECs conditions are investigated using single cells.

2. Experimental

2.1. Powder preparation

The selected compositions of the $Pr_2Ni_{1-x}Co_xO_{4+\delta}$ ($x = 0.0$, 0.1 and 0.2) were prepared using a solid state synthesis route. The corresponding precursors were Pr_6O_{11} (Aldrich chem, 99.9%), NiO (Alfa Aesar, 99%) and Co_3O_4 (Alfa Aesar, 99%). Pr_6O_{11} powder was pre-fired in a first step at $T = 900$ °C overnight to remove the water content, due to its high hygroscopic character. The precursors were weighed according to the composition of nickelates and then ball milled for 4 h at 250 rpm using zirconia balls and isopropanol (VWR, 99.8%). Subsequently drying at 80 °C overnight, the final annealing was performed at 1300 °C for 12 h in air in order to get pure and well crystallized phases. After crushing the powder, further milling was carried out using zirconia balls and isopropanol for 8 h with the aim to obtain a mean particle size of about 1 μm.

2.2. X-ray diffraction analysis

The synthesized powders were first examined by X-Ray diffraction (XRD) at room temperature using a PANanalytical X'pert MPD diffractometer with Cu-K_α incident radiation to check the purity of phase. In the next step, each X-ray diffractogram was fitted by profile matching using the Fullprof software and Rietveld Refinements were carried out.

2.3. Microstructure, particle size and surface area analysis

A Scanning Electron Microscope (Quanta FEG 650, FEI equipped with an EDS detector) was used to investigate the morphologies of the powders as well as the microstructures of the cell. The particle size distributions were analyzed by laser diffraction particle size analyser (HORBIA, LA-960). The specific surface areas of the materials were obtained with a Brunauer – Emmet – Teller (BET) analysis system with N_2 adsorptive medium (QUADRASORB) at a temperature of 77 K.

2.4. Thermo gravimetric analysis (TGA)

In order to determine the delta value, δ, at room temperature under air, TGA experiments were carried out using a TA Instrument® TGA-5500 device. First the powders were equilibrated under air up to 600 °C, then cooled down to room temperature with a slow rate (2 °C·min^{-1}), this cycle being reproduced twice to ensure a stable state of the material, *i.e.* a reproducible oxygen content. Then, a second cycle was performed under Ar - 5% H_2 flux with a very slow heating rate of (0.5 °C·min^{-1}), the decomposition of the material leading to the determination of the oxygen stoichiometry after cycling the sample down to room temperature (Pr_2O_3, metallic Ni and Co being formed as verified by XRD after the thermal cycle).

2.5. Cell preparation

For the electrochemical characterization the symmetrical half-cells, electrode//GDC//8YSZ//GDC//electrode were prepared. Terpineol-based slurries were prepared with gadolinium doped ceria *i.e.* $Ce_{0.8}Gd_{0.2}O_{2-\delta}$ (GDC) powder (CerPoTech) and with each nickelate material. The GDC layers (thickness ~ 3–4 μm, ∅ ~ 12 mm) were first symmetrically screen printed on both sides of the dense supports of 8 mol% of yttria stabilized zirconia (8YSZ) with diameter ~20 mm and thickness ~300 μm and sintered at 1350 °C for 1 h under air. This dense and thin GDC buffer layer was deposited to avoid the reactivity between electrode and 8YSZ electrolyte [17]. The oxygen electrode *i.e.* the nickelate layer (∅ ~ 10 mm, thickness ~ 15–20 μm) was afterwards symmetrically deposited on the both sides of GDC//8YSZ//GDC substrate and sintered at 1150 °C for 1 h under air. This sintering temperature was optimized for PNO, with the aim to obtain a controlled

homogenous porous electrode microstructure. Later on, the same sintering conditions were used for preparing the Co-substituted nickelates electrode.

2.6. Electrochemical characterization

The electrochemical measurements of symmetrical cells were performed using a two electrodes configuration with signal amplitude of 50 mV under zero dc current conditions.

The single cell measurements were performed using NiO-YSZ supported cells (NiO-YSZ//YSZ//GDC//electrode, CeramTec®, ASC-10C type). Oxygen electrode layers *i.e.* nickelates were deposited by screen printing and sintered at 1150 °C for 1 h under air. Finally, a $LaNi_{0.6}Fe_{0.4}O_{3-\delta}$ (LNF) layer (∅ = 10 mm) was deposited to improve the current collection [26]. For the electrochemical measurement, Gold and Nickel grids (1.024 cm^{-2} mesh) were used as current collectors for oxygen electrode and fuel electrode respectively. The current density-voltage (*i-V*) characteristic was measured in electrolysis mode from OCV to 1.5 V with a 50% H_2O and 50% H_2 gas mixture in the temperature range of 700–900 °C. The impedance diagrams were recorded at OCV and from 1.0 to 1.5 V with an increase of 0.1 V, under potentiostatic control with 50 mV *ac* amplitude, from 10^6 Hz down to 10^{-1} Hz, using an IVIUM VERTEX potentiostat/galvanostat with integrated frequency response analyser module. The distribution of relaxation times (DRT) analysis was performed with the intention to find the number of time constants present in the impedance spectrum. The complex impedance diagrams were fitted using an equivalent circuit models by means of the RelaxIS® software. The polarization resistance R_p values were calculated from the difference between the low frequency (LF) and the high frequencies (HF) diagram intercepts with the real axis of the Nyquist representation.

3. Results and discussion

3.1. XRD analyses

The X-ray diffraction analysis of the as-synthesized powder indicate that all three nickelates *i.e.* $Pr_2Ni_{1-x}Co_xO_{4+\delta}$ (x = 0.0, 0.1 and 0.2) are single phases and all diffractograms can be indexed with an orthorhombic cell described by the *Fmmm* space group. The nickelates with more than 20% cobalt content were not considered in this work due to instability of the layered structure in air/oxygen atmosphere. The full pattern profile matching was carried out using the FULLPROF software with the aim to extract the lattice parameters. A decent agreement is observed between the experimental and refined patterns. The XRD profile matching of $Pr_2NiO_{4+\delta}$ (PNO, χ^2 = 2.46), $Pr_2Ni_{0.9}Co_{0.1}O_{4+\delta}$ (PNCO10, χ^2 = 2.41) and $Pr_2Ni_{0.8}Co_{0.2}O_{4+\delta}$ (PNCO20, χ^2 = 2.48) are shown in Fig. 1. The cell parameters and unit cell volume of all PNCO phases are listed in Table 1.

A slight increase in the lattice parameters a and b is observed whereas a decrease is observed in the lattice parameter c. The large decrease in parameter c compared to the increase in a and b leads to a decrease of the overall cell volume. This observance is most likely due to smaller ionic radius of Co^{2+} (0.65 Å) than that of Ni^{2+} (0.69 Å) [24], that causes a decrease in bond length between B-site cation and oxygen. A similar observation *i.e.* a decrease in the volume with cobalt substitution at Ni-site is reported for other layered perovskite $La_2Ni_{1-x}Co_xO_{4+\delta}$ [27] as well as for simple perovskites $La_2Ni_{1-x}Co_xO_{3-\delta}$ based compounds [28].

3.2. Thermo gravimetric analysis

3.2.1. Determination of δ of material equilibrated under air

The δ value *i.e.* the oxygen over-stoichiometry for PNCO compounds at room temperature was determined using the TGA experiments performed under reducing conditions (Ar−5% H_2 atmosphere, with a slow heating rate of 0.5 °C·min^{-1}) after equilibrated in air. Fig. 2a depicts the

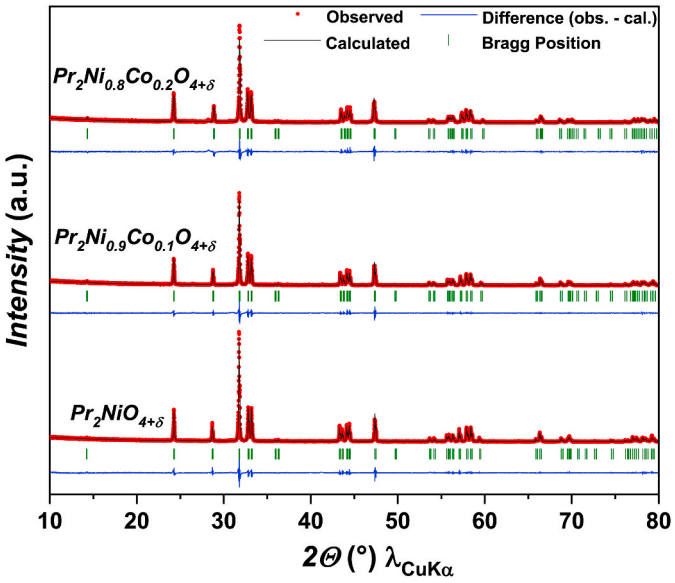

Fig. 1. Fullprof refinement of X-ray diffraction patterns of $Pr_2NiO_{4+\delta}$ (χ^2 = 2.46), $Pr_2Ni_{0.9}Co_{0.1}O_{4+\delta}$ (χ^2 = 2.41) and $Pr_2Ni_{0.8}Co_{0.2}O_{4+\delta}$ (χ^2 = 2.48) using *Fmmm* space group.

Table 1
Lattice parameters a, b, c and space groups of $Pr_2Ni_{1-x}Co_xNiO_{4+\delta}$.

Samples	a (Å)	b (Å)	c (Å)	V (Å^3)	Space Group
$Pr_2NiO_{4+\delta}$	5.394 (3)	5.454 (3)	12.443 (3)	366.17 (3)	*Fmmm*
$Pr_2Ni_{0.9}Co_{0.1}O_{4+\delta}$	5.399 (3)	5.460 (4)	12.407 (2)	365.76 (3)	*Fmmm*
$Pr_2Ni_{0.8}Co_{0.2}O_{4+\delta}$	5.403 (4)	5.465 (4)	12.369 (3)	365.28 (3)	*Fmmm*

variation of weight loss as a function of temperature. Mainly two weight losses are observed similar to other earlier reported K_2NiF_4-type nickelates [27,29]. The first weight loss around 400 °C, corresponds to the reduction of M^{3+} (Ni^{3+}/Co^{3+}) into M^{2+} (Ni^{2+}/Co^{2+}) (*i.e.* δ = 0 when expecting only Pr^{3+} cations). The second weight loss describes the complete reduction of PNCO into appropriate ratio of Pr_2O_3, Ni and Co confirmed by XRD, resulting to the determination of δ value.

$$Pr_2Ni_{1-x}CoxO_{4+\delta} \xrightarrow{H_2} Pr_2Ni_{1-x}Co_xO_4 + \delta\, H_2O \quad (1)$$

$$Pr_2Ni_{1-x}Co_xO_4 \xrightarrow{H_2} Pr_2O_3 + (1-x)\,Ni + x\,Co + H_2O \quad (2)$$

The similar δ value is obtained from first and second plateau according to the reaction 1 and 2, respectively. The value of δ was also determined by iodometric titration [22]. The δ values calculated by TGA and Iodometry are summarized in Table 2. It can be pointed out, as expected, that the δ value increases from 0.24 (PNO) to 0.29 (PNCO20) with Co substitution (Fig. 2b). This increase in δ value can be attributed due to increasing M^{3+} content (Fig. 2b). In addition to TGA and Iodometry titration, the XPS measurements were carried out in order to analyse the elemental valence of Ni/Co, the results are presented in Supplementary Information Fig. S1. However, the complex nature of the Ni2p3/2 peak [30] prevents the deconvolution and the quantification of Ni^{2+} and Ni^{3+} oxidation state. Moreover, the Co2p3/2 peaks are not clearly visible due to a strong interference from the PrMNN peak, which is highly intense because of much higher proportion of Pr compared to Co in the sample (*cf.* Fig. S1).

The obtained δ values in this work for PNO is in good agreement with the earlier reported results [9]. Usually, by increasing the oxygen

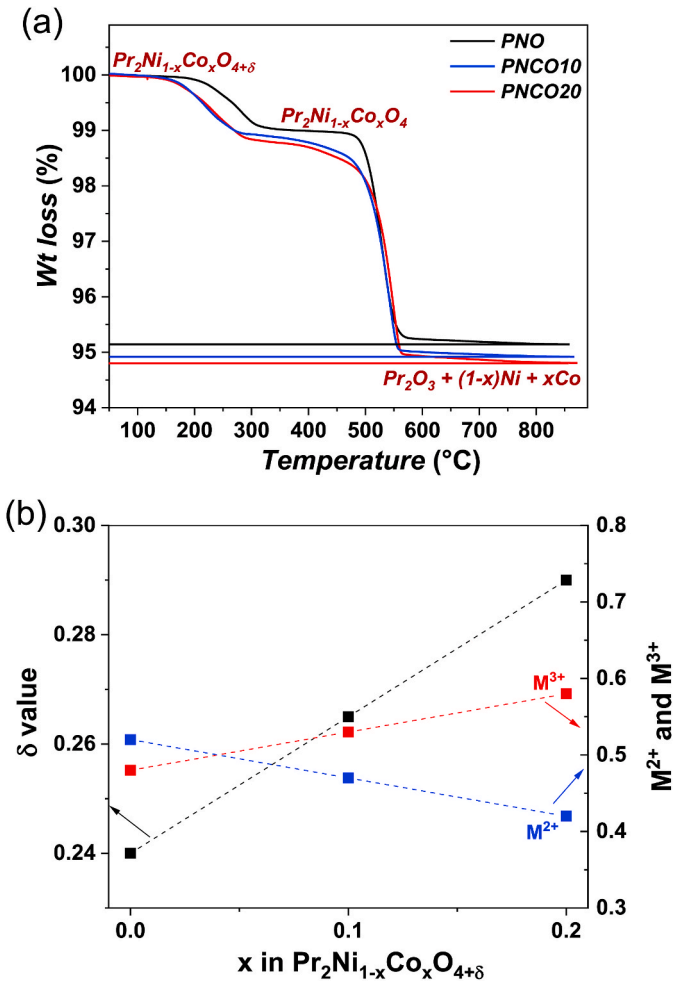

Fig. 2. (a) Weight loss curve in Ar-5%H_2 atmosphere and (b) thermal variation of the oxygen over-stoichiometry δ-value, $M^{2+}(Ni^{2+}/Co^{2+})$ and $M^{3+}(Ni^{3+}/Co^{3+})$ content for $Pr_2Ni_{1-x}Co_xO_{4+\delta}$ compounds.

Table 2
Oxygen over-stoichiometry δ calculated from TGA and iodometry measurements, and the average δ value.

Nickelates	δ (by TGA)	δ (by Iodometry)	δ (average)
$Pr_2NiO_{4+\delta}$	0.25	0.23	0.24
$Pr_2Ni_{0.9}Co_{0.1}O_{4+\delta}$	0.27	0.27	0.27
$Pr_2Ni_{0.8}Co_{0.2}O_{4+\delta}$	0.30	0.28	0.29

over-stoichiometry (δ), the ionic transport properties like oxide ion diffusivity/ionic conductivity is increased [9]. Therefore, the increase in δ value with increasing cobalt content could be the first indication towards the better electrochemical properties of these compounds.

3.3. Electrochemical measurements

3.3.1. Morphology, particle size and surface area of powders

Before the preparation of screen-printing paste, the morphology of the as prepared powder for all three compositions of PNCO was investigated by SEM (*cf.* Fig. S2). As obvious, the particle size is about several micrometers and formed big agglomerates. In fact, the very high calcination temperature leads to larger particle size and aggregates. Therefore the obtained powders were ball milled with zirconia balls in isopropanol for 8 h, to get smaller and homogeneous particles of around 1 μm (confirmed by SEM). The particle sizes were also investigated by laser diffraction particle size analyser and the results are in good agreement with the SEM results.

The specific surface area of the as prepared and milled powders was measured by BET. The initial surface area *i.e.* for as prepared powder was ~0.2–0.25 $m^2 \cdot g^{-1}$ for all three compositions. However, the surface area significantly enhanced to 2.96, 3.17 and 2.51 $m^2 \cdot g^{-1}$ respectively for PNO, PNCO10 and PNCO20 after 8 h milling.

3.3.2. Symmetrical half-cells measurements

The symmetrical cell containing PNCO electrode was mounted into the measurement setup, with flow of air. The cell was heated at 900 °C in order to achieve good contact and then the impedance diagrams were recorded by EIS at $i_{dc} = 0$ condition in the temperature range 700–900 °C under air.

All the impedance spectra were first analyzed using the distribution of relaxation time (DRT) method [31–36]. According to the DRT analysis, mainly two time constants are observed for PNO and PNCO20 symmetrical half-cells, as shown in Supplementary Information Fig. S3. Therefore, the fitting of impedance diagrams for all the PNCO half-cells were carried out with two *R||CPE* (constant phase element) in series along with a series resistance R_s. This is the simplest equivalent circuit model that yields a good fit to the data (Fig. 3 a, b).

The data analysis shows a decrease in R_p for cobalt substituted PNO electrodes. For instance, a R_p value of 66 mΩ·cm^2 is achieved at 800 °C for PNO while after substitution of Ni by Co, the R_p values decrease down to 58 mΩ·cm^2 for PNCO20 (Fig. 3 a, b). The observed R_p value for PNO symmetrical half-cell is slightly higher than that of previously reported results [9]. This might be caused by a different synthesis route as well as a difference in the particle size. No electrochemical data is available in the literature for electrochemical performance of cobalt substituted nickelates. Therefore, from these preliminary results, it can be concluded that the best electrochemical property (*i.e.* lowest R_p) is achieved with the PNCO20 electrode.

According to the impedance data analysis, the electrode response is composed of two main contributions located at medium frequency (~10–100 Hz) and low frequency (~0.2–1 Hz), independent of the composition of the electrodes (Supplementary Fig. S3). In general, the medium frequency arc resistance can be associated with various electrode processes such as the adsorption/desorption of gaseous O_2, dissociation/association of O_2 and charge transfer-diffusion (O^{2-}) in the electrode [37–39]. The low frequency arc can be related to gas diffusion impedance due to either porous electrodes or the experimental set-up [40–42]. To further investigate the rate limiting step among these electrode processes as well as the influence of cobalt substitution on the electrode reaction mechanism, the impedance analysis under different oxygen partial pressures (pO_2) were carried out.

3.3.3. Investigation of rate limiting step

The variations of impedance spectra with pO_2 at 800 °C for PNO and PNCO20 symmetrical half-cell are plotted in Fig. 4a and b. As expected, an increase in total polarization resistance is observed with decreasing pO_2. A 3D-DRT analyses of these impedance curves are shown in Fig. 4c and d. The X-axis is recalculated to frequency in Hz instead of time in seconds whereas the oxygen partial pressures is plotted on Y-axis. Two peaks are mainly detected, one around 1–100 Hz (process P_1) and the other one around 1 Hz (process P_2), independent of cobalt content. The resistance corresponding to process P_1 is always higher than that of P_2 and both of them are decreasing with increasing the pO_2. A slight shift of process P_1 towards higher frequency is also noticed with increasing pO_2. In addition, two processes are always detected throughout the temperature range of 700–900 °C. The 3D-DRT analysis of the impedance spectra (under air at OCV conditions) as a function of temperature are reported in the Supplementary Information Fig. S4. With increasing the temperature, the peak position of process P_1 is shifting towards higher frequency while the process P_2 always remain at the same frequency. In addition, at lower temperature especially at 700 °C, the process P_2 merges with the process P_1. Moreover, the resistance of process P_1 is

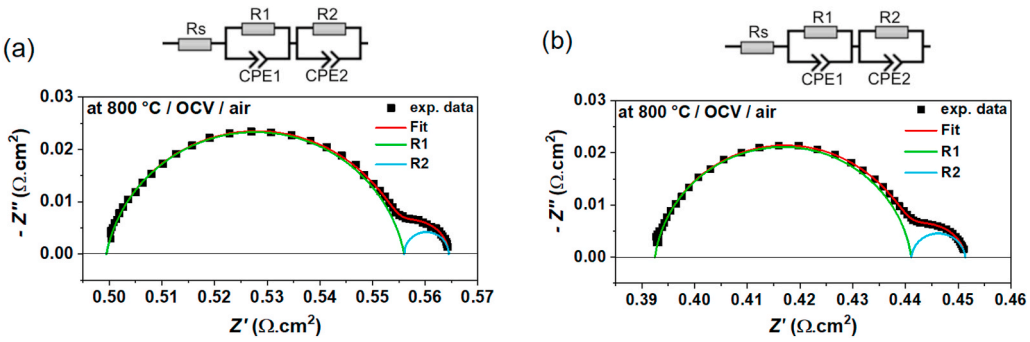

Fig. 3. Impedance spectra at 800 °C and their fitting using two *R||CPE* elements for (a) PNO and (b) PNCO20 symmetrical half-cells.

decreasing while the process P_2 remains almost independent with increasing temperature, clearly indicates that the process P_1 is the thermally activated process while the process P_2 is not. The non-activation of the process P_2 with temperature further points towards a diffusion process.

Therefore, we introduced two time constant to fit all of our impedance data using two *R||CPE* elements along with a series resistance R_s in order to determine the resistance associated with the two individual processes (P_1 and P_2). The impedance data analysis as a function of temperature at OCV conditions reveals that the resistance of process P_2 for both PNO and PNCO20 cells is almost constant ~0.01 Ω·cm^2 however the R_p of process P_1 is decreased with increasing temperature from 700 to 900 °C. For instance, the R_p values for process P_1 are 0.25, 0.10, 0.045, 0.03 and 0.015 Ω·cm^2 at 700, 750, 800, 850 and 900 °C respectively for PNO symmetrical cell. In case of PNCO20 symmetrical cell, the R_p values for process P_1 are 0.22, 0.096, 0.04, 0.02 and 0.01 Ω·cm^2 at 700, 750, 800, 850 and 900 °C respectively. These values of R_p for processes P_1 and P_2 were further confirmed by determining the area under different DRT peaks.

Typically, the resistance (R_n) of individual electrode process under open circuit voltage (OCV) conditions, strongly depends on the partial pressure. The experimental data can be fitted with a power law according to the following relation,

$$R_n \propto (pO_2)^{-m}$$

In the above equation, the exponent m describes the nature of the step involved in the electrochemical reaction and depend on the kinetic limiting step [43,44]. According to the literature [45–48], the most common values of m are 0, 0.25, 0.5 and 1. By considering the oxygen evolution reaction at the electrode, the value of m can be described as follows:

$m = 0$, describes the ionic transfer of O^{2-} ions through the electrolyte-electrode interface and diffusion of O^{2-} oxide ions:

$$O^{2-}{}_{(electrolyte)} \Leftrightarrow O^{2-}{}_{(electrode)}$$

$m = 0.25$ corresponds to the oxygen surface exchange reaction (*i.e.* charge transfer process), occurs usually at the two-phase gas/electrode interface; it involves the oxidation of O^{2-} ions and the adsorption of oxygen at the surface of electrode

$$O_O^x \Leftrightarrow O^{2-}{}_{ads} + V_O^{\bullet\bullet}$$

$$O^{2-}{}_{ads} \Leftrightarrow O_{ads} + 2e^-$$

$m = 0.5$ is associated to the mass transport *i.e.* association of the desorbed atomic species (O_{ads}) into molecular oxygen ($O_{2,ads}$) at the electro-active sites of the MIEC oxide.

$$2\ O_{ads} \Leftrightarrow O_{2,ads}$$

$m = 1$ describes the desorption of $O_{2,ads}$ at the active reaction sites and then the diffusion of gaseous oxygen O_2(g) within the pores or above the electrode.

$$O_{2,ads} \Leftrightarrow O_2\ (g)$$

In addition to the above mentioned values of m, some intermediate values have been also reported. For instance, $m = 3/8$ (0.375), describes the charge transfer in competition with an oxygen mass transport [44] and $m = 1/8$ (0.125) describes further release of electrons by O^{2-} (*i.e.* $O^{2-}{}_{(electrode)} \Leftrightarrow O^{-}{}_{(electrode)} + e^-$) [49,50].

In this work, we also attempted to investigate the slope of individual process. The variations of R_p of two process P_1 and P_2 (*i.e.* R_1 and R_2) as a function of pO_2 are represented in Fig. 4e. Two different exponents *i.e.* m values are obtained subsequently carrying out linear fitting to the two different polarization resistance R_1 and R_2 for both PNO and PNCO20 symmetrical half-cells.

In our case, the exponents $m \sim 0.25$ and 1 indicate that the oxygen surface exchange reaction *i.e.* charge transfer process (surface diffusion of the adsorbed/desorbed oxygen atoms and their consequent reduction/evolution) and the gas diffusion process, respectively are involved in the electrode reaction process for both PNO and PNCO20 symmetrical half-cells. This is in good agreement with the earlier reported result for PNO [42]. Regardless the substitution with cobalt at Ni site in PNO did not show any change the electrode process. Furthermore, the polarization resistance R_1 is always higher compared to R_2 throughout the pO_2 range (Fig. 4e) clearly indicates that the charge transfer process is the rate limiting step among the electrode process for these PNO and Co substituted PNO electrodes.

3.3.4. Single cell measurements

To perform the electrochemical measurement, the single cell was mounted into the measurement setup and heated at 900 °C, with flows of compressed air and N_2 on the oxygen and fuel electrode sides, respectively. The flow of N_2 at the fuel side was progressively substituted by dry hydrogen (H_2) to reduce NiO into metallic Ni. After complete reduction of the single cell, the OCV under dry condition (9 NL·h^{-1} H_2 and 9 NL·h^{-1} air, on fuel electrode side and oxygen electrode side respectively) was ≈ 1.21 V at 900 °C for all three cells indicating a leakage across the gasket below 0.3%. Under humidity *i.e.* with 50% H_2 and 50% H_2O mixture (4.5 NL·h^{-1} H_2 + 4.5 NL·h^{-1} H_2O and 9 NL·h^{-1} air, on fuel electrode side and oxygen electrode side respectively), the measured OCVs are 0.95, 0.94 and 0.92 V at 800, 850 and 900 °C, respectively, for PNO single cells. These values are close to the theoretical OCV values. Similar OCVs were also observed for the cobalt substituted PNO *i.e.* PNCO10 and PNCO20 cells.

The typical current-voltage characteristics of PNCO single cells at 800 and 900 °C are shown in Fig. 5. The increase in electrochemical performance is observed with increasing the cobalt content in PNO electrode, independent of the temperature. The maximum current densities obtained under the applied voltage of 1.5 V at 900 °C are 3.0, 2.4 and 2.1 A·cm^{-2} respectively for PNCO20, PNCO10 and PNO single cells, and at 800 °C, the current densities are 1.90, 1.75 and 1.60 A·cm^{-2}

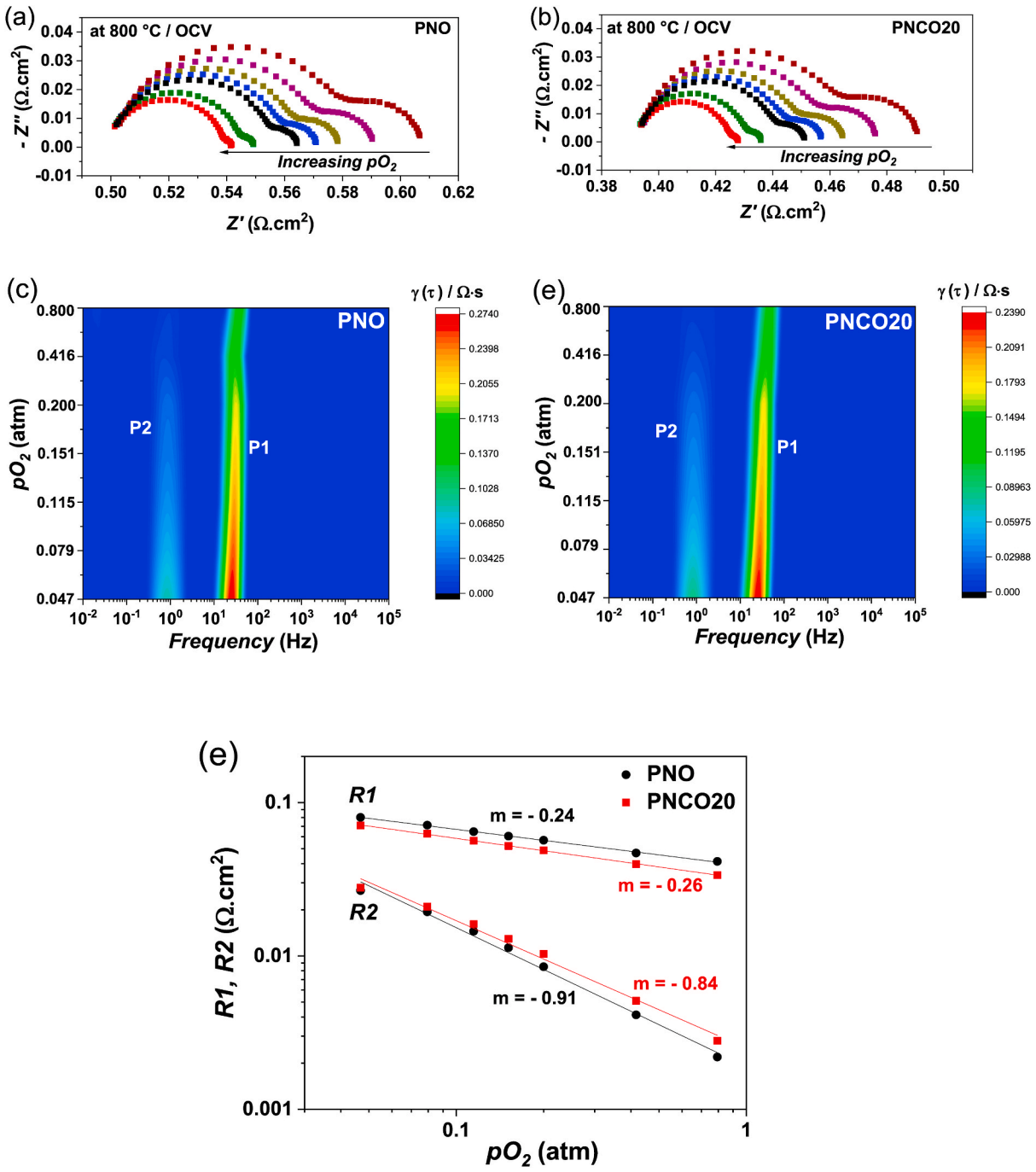

Fig. 4. Variation of impedance spectra at OCV (a, b), DRT (c, d) and polarization resistances (e) (the error bars are within the data symbol), as a function of oxygen partial pressure for PNO and PNCO20 symmetrical half-cells at 800 °C.

respectively for PNCO20, PNCO10 and PNO single cells (Fig. 5). Remarkably, the performance of the cell is improved continuously with increasing the cobalt content in PNO electrode. Indeed similar behaviour *i.e.* a decrease in total R_p with increasing cobalt content was also observed for the symmetrical half-cells containing PNCO electrodes. The best electrochemical performance is thus observed for the single cell with PNCO20 electrode. The improvement in the performance with cobalt could be due to the enhancement in the transport properties, mainly the diffusion coefficient (D^*) and surface exchange coefficient (k^*). Recently, Berger *et al.* have reported the behaviour of PNO and PNCO10 thin film microelectrodes on YSZ substrates and investigated that the surface exchange coefficients of PNCO10 is higher than that of PNO especially for $pO_2 \leq 0.21$ [51]. Similar trend was also reported by Kilner *et al.* and Munnings *et al.* for cobalt substituted $La_2NiO_{4+\delta}$ (LNO) [20,29]. The substitution with cobalt in LNO slightly improves the diffusion coefficient but essentially enhances the surface exchange coefficient of the material with significantly lower activation energy. We have recently reported the improvement in the electrochemical activity for cobalt substituted LNO electrodes [27]. Hence, these properties are directly linked with the electrochemical properties of the materials [52] and shows an enhancement in the electrochemical performance of the cells containing cobalt doped nickelate oxygen electrode.

As shown in Fig. 5, the performance of PNCO electrodes containing single cells were compared with the commercial single cell containing LSCF state of art oxygen electrode. Remarkably, the cobalt substituted PNO electrode containing single cells show higher cell performance than

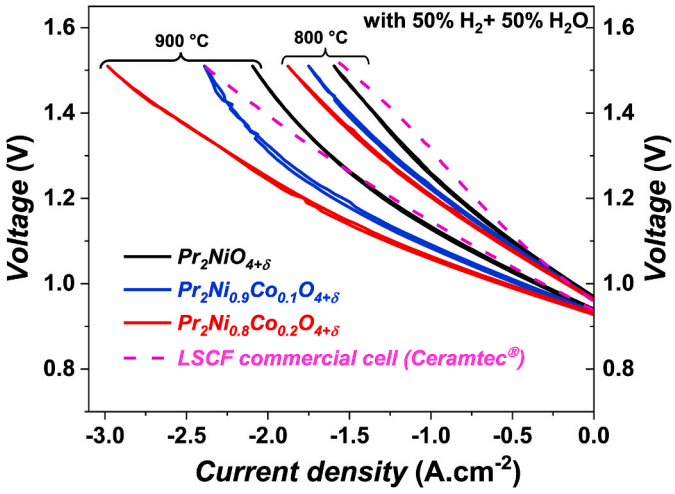

Fig. 5. Voltage *vs.* current density curves for the single cells containing PNO, PNCO10, PNCO20 and LSCF electrodes at 800 and 900 °C.

that of LSCF cell. Indeed the performance of PNCO20 cell is very high as compare to the other data available in the literature for SOECs [14, 53–55].

The impedance diagram (Nyquist plots) of PNO and PNCO20 single cells at 800 °C under OCV conditions (with 50% H_2 and 50% H_2O feed gas mixture at fuel electrode) are reported in the Supplementary Information Fig. S5. The two cells have almost identical series resistance but the cell with PNCO20 electrode shows lower R_p. The R_p value of 128 and 118 mΩ·cm^2 are obtained for PNO and PNCO20 electrode containing single cells, respectively at 800 °C under OCV condition. As expected, the R_p values measured on single cells are higher than that of symmetrical cell (66 mΩ·cm^2 and 58 mΩ·cm^2 for conventional PNO and PNCO20 electrode containing symmetrical half-cells), as the contribution of cathode *i.e.* the fuel electrode is also appearing in single cell. The 3D-DRT plots of the single cells at OCV conditions as a function of temperature are depicted in Supplementary Information Fig. S6. It is clear that the oxygen electrode reaction process are affected by the fuel electrode. At least four process (P_1, P_2, P_3 and P_4) is observed for both PNO and PNCO20 single cells. The middle-frequency process P_3 is believed to be the contributions from the oxygen electrode as it appears around the same frequency range (~1–100 Hz) as that of process P_1 (*cf.* Fig. S4) of the symmetrical half-cells. However, from the width of the intensities, there might also be contributions from the fuel electrode. It seems that, at temperature <750 °C, the process P_4 merges with the process P_3. The high-frequency process P_1 (~10^3–10^4 Hz), another middle frequency (~10^2–10^3 Hz) process P_2, and the low frequency (around 5 Hz) process P_4 could be the contributions from the fuel electrode.

Additionally, the total cell resistances *i.e.* ASR values were calculated as a function of applied potential in 700–900 °C temperature range for all three cells. The ASR is dependent on both applied potential and operating temperature *i.e.* an increase is observed with increasing applied potential and decreasing the cell temperature. The ASRs of PNO and PNCO20 cells at 800 and 900 °C are compared in Supplementary Information Fig. S7. Nevertheless, it can be clearly discerned that the ASR of PNCO20 cell is always lower than that of PNO cell whatever the applied potential and temperature range. For instance, the ASR value at 1.3 V is 0.27 and 0.32 Ω·cm^2 at 800 °C respectively for PNCO20 and PNO single cell. The variation of ASR values of all these cells are consistent with the slope of *i-V* curves.

3.3.5. Short term durability test

The short-term durability tests up to 250 h with PNCO single cells were galvanostatically carried out at 800 °C under steam electrolysis conditions. The feed gas mixture of 50% H_2, 50% H_2O with a total flow of 9 NL·h^{-1} was introduced to the fuel electrode. The stability of the single cells (represented in terms of cell voltage) at a constant current load of −1 A·cm^{-2} as a function of operation time are shown in Fig. 6. The initial cell voltage (at t = 0) is slightly higher than presented in the *i-V* curves of Fig. 5. This might be due to the fact that the cells already spent ~ 60–72 h at high temperature under electrolysis conditions (due to the measurement at other temperatures) before starting the stability test.

In SOEC mode, all three cells experienced different degradation during the stability test. At the beginning, all these cells display a rapid increase in the electrolysis voltage and then show a stable behaviour. For instance, an increase in voltage from 1.30 to 1.37 V is observed for PNO cell after 250 h, indicates the highest degradation among all. Furthermore, the degradation rate (in mV·kh^{-1}) can be estimated from the Voltage *vs.* Time curve by carrying out linear fit in the stability region. In this way a degradation rate of ~ 88 mV·kh^{-1} is observed for PNO single cell. However, the other two cells show lower degradation rates, the electrolysis voltage increased from 1.28 to 1.33 V (~ 36 mV·kh^{-1}) and 1.27–1.30 V (~ 22 mV·kh^{-1}) for PNCO10 and PNCO20 single cell respectively. The short term durability of PNCO electrodes containing single cells were also compared with the commercial single cell containing LSCF state of art oxygen electrode. The LSCF cell shows almost similar degradation rate (*i.e.* ~ 87 mV·kh^{-1}) like PNO single cell. Remarkably, the cobalt substituted PNO electrode containing single cells show comparatively lower degradation rates than that of LSCF cell.

Finally, it must be emphasised that the PNCO20 single cell displays lowest degradation after 250 h under electrolysis conditions. Therefore, in the next step, the post-test analysis were carried out with these cells to understand different behaviour during stability test.

3.3.6. Post-test analysis of the single cells

After performing the stability test, the single cells were embedded in resin and polished along the cross-section prior to SEM-EDAX analyses. The analyses were mainly focused on electrolyte, electrolyte/GDC interface, GDC/electrode interface and bulk of oxygen electrodes expecting the same behaviour/degradation of fuel electrode in all three cells. Fig. 7 compares the electrolyte//GDC//electrode interfaces before and after 250 h operation at −1 A·cm^{-2} under steam electrolysis condition at 800 °C, for PNO and PNCO20 single cells.

It must be point out that no severe damage or delamination/cracks were observed for all the cells. In addition, almost no change is observed at the electrolyte/GDC or GDC/electrode interface before and after the stability test for all PNCO cells. However, for the PNO cell, a partial

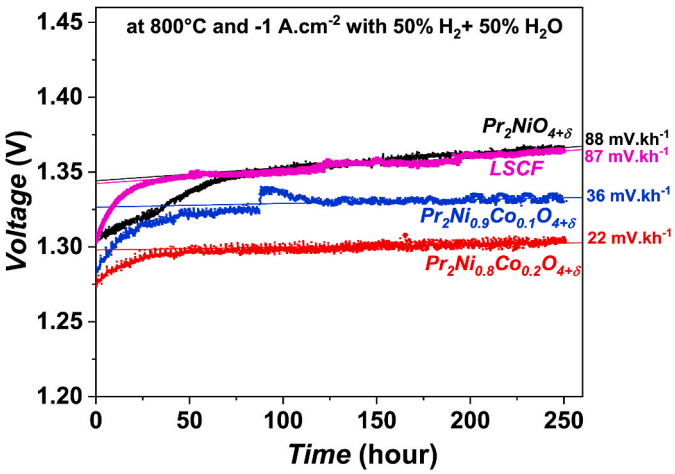

Fig. 6. Stability of PNO, PNCO10, PNCO20 and LSCF single cells at 800 °C under current density of −1 A·cm^{-2} with 50% H_2 + 50% H_2O feed gas mixture.

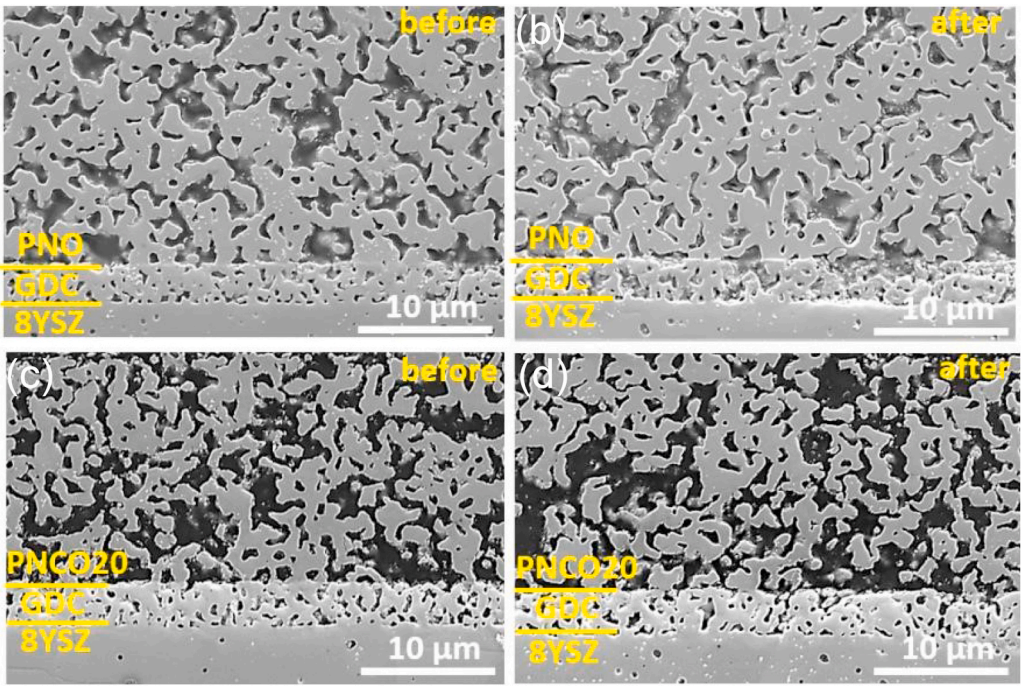

Fig. 7. SEM images after 250 h of operation for PNO and PNCO20 single cells before and after the stability test at 800 °C with a current load of −1 A·cm^{-2} and 50% H_2 + 50% H_2O feed gas mixture.

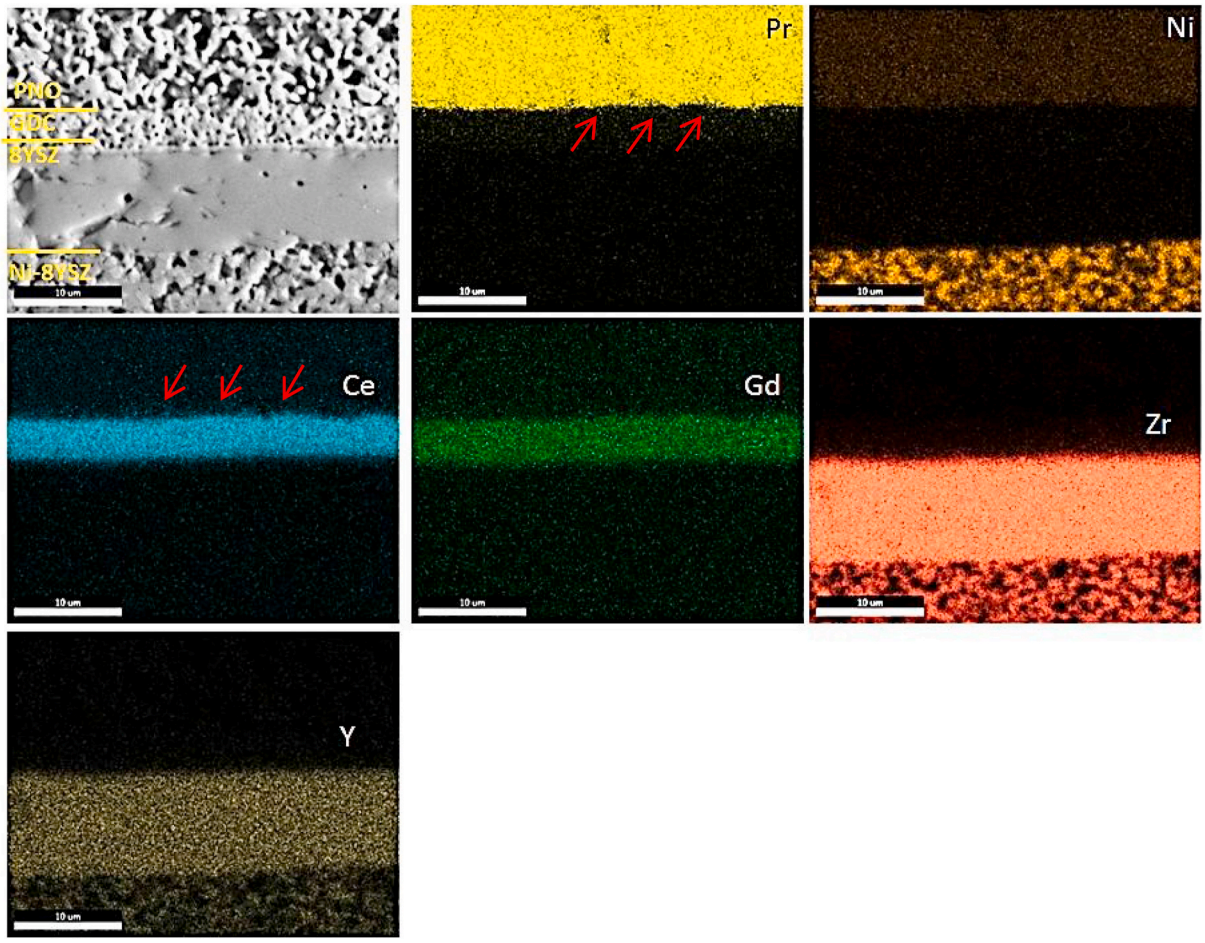

Fig. 8. Elemental mapping at the cross-section of PNO//GDC//8YSZ//Ni-YSZ cell after 250 h operation under electrolysis at −1 A·cm^{-2} with 50% H_2 + 50% H_2O gas mixture.

roughness or pore formation is observed in the GDC layer (Fig. 7b). Moreover, partial coarsening of the electrode is also noticed for the PNO cell. These alterations were not observed for the PNCO20 cell and could be the reason for the large degradation for the PNO single cell.

In order to get further information, the SEM-EDAX mapping was performed on the cross-section of the PNO//GDC//8YSZ//Ni-YSZ cells. The SEM image with the corresponding atomic concentration mapping for Pr (L_α, 5.03 keV), Ni (K_α, 7.47 keV), Co (K_α, 7.93 keV), Ce (L_α, 4.84 keV), Gd (L_α, 6.06 keV), Zr (L_α, 2.04 keV), Y (L_α, 1.92 keV) is shown in Fig. 8. All the elements are located in the phase where they are expected and no cation segregation is observed. Nevertheless, partial Ce diffusion from the GDC layer to the PNO electrode and also some Pr diffusion from electrode to the GDC layer is observed, resulting in the formation of an interphase between the GDC and the PNO electrode. The SEM-EDX mapping on the cross section of PNCO20//GDC//8YSZ//Ni-YSZ cell was also performed and reported in the Supplementary Information Fig. S8. Like PNO cell, cation segregation is also not detected for the PNCO20 cell. However, the inter-diffusion of Ce and Pr at the electrode//GDC interface seems similar as that of the PNO cell.

The reactivity of PNO and GDC is already known in the literature [56,57]. At elevated temperature (≥900 °C) they react and form various phases including $Pr_4Ni_3O_{10+\delta}$, Pr_6O_{11} and Pr-doped GDC. The previous reported results show that all these phases are good MIEC oxide materials and hence might be less detrimental for the electrochemical performance and for the durability of the SOECs [15,58–61].

4. Conclusion

The present study is focused on the finding of alternative oxygen electrodes for SOECs. In this respect $Pr_2Ni_{1-x}Co_xO_{4+\delta}$ ($x = 0.0$, 0.1 and 0.2) (PNCO) nickelates were considered and successfully synthesized. These nickelates exist with orthorhombic structure with *Fmmm* space group. A continuous increase in the oxygen over-stoichiometry δ value is observed with increasing x *i.e.* with increasing cobalt content. The EIS measurements of symmetrical half-cells show lower R_p values for $Pr_2Ni_{0.8}Co_{0.2}O_{4+\delta}$ (PNCO20) compare to that of $Pr_2NiO_{4+\delta}$ (PNO) cell. However, the electrode reaction mechanism remains the same and among the electrode processes, the charge transfer process is the rate limiting step for both electrodes. With respect to single cells, most importantly, an increase in electrochemical performance is observed with cobalt substitution. The highest current densities *i.e.* 3.0 and 1.9 $A{\cdot}cm^{-2}$ at 900 and 800 °C respectively, are observed for PNCO20 single cell which is better than that of state of art LSCF oxygen electrode containing single cell. Through the stability test up to 250 h at 800 °C and -1 $A{\cdot}cm^{-2}$ current load, a higher degradation rate is observed for PNO single cell compared to cobalt substituted PNO single cell. More especially for the $_{PNCO20}$ single cell, a stable behaviour ($\sim$22 $mV{\cdot}kh^{-1}$) is observed with slight increase in electrolysis voltage. Hence $Pr_2Ni_{0.8}Co_{0.2}O_{4+\delta}$ (PNCO20) electrode can be consider as a potential oxygen electrode for SOECs.

CRediT authorship contribution statement

V. Vibhu: Methodology, Investigation, Formal analysis, Validation, Writing - original draft, Writing - review & editing. **I.C. Vinke:** Supervision, Funding acquisition, Project administration. **R.-A. Eichel:** Funding acquisition, Project administration. **L.G.J. de Haart:** Supervision, Funding acquisition, Project administration.

Declaration of competing interest

The authors declare that they have no known competing interests or personal relationships that could have appeared to influence the work reported in this paper.

Acknowledgments

The results reported here were obtained within the frame of the European project SElySOs. This project has received funding from the Fuel Cells and Hydrogen 2 Joint Undertaking under grant agreement No 671481. This Joint Undertaking receives support from the European Union's Horizon 2020 research and innovation programme and Greece, Germany, Czech Republic, France, Norway. The authors also acknowledge to H. Hartmann and A. Besmehn from the Central Institute for Engineering, Electronics and Analytics, ZEA-3, Forschungszentrum Jülich GmbH for the XPS measurements and Ansgar Kretzschmar for the BET measurements.

Appendix A. Supplementary data

Supplementary data to this article can be found online at https://doi.org/10.1016/j.jpowsour.2020.228909.

References

[1] S.H. Jensen, P.H. Larsen, M. Mogensen, Int. J. Hydrogen Energy 32 (2007) 3253–3257.
[2] J. Udagawa, P. Aguiar, N.P. Brandon, J. Power Sources 166 (2007) 127–136.
[3] Y. Song, X. Zhang, K. Xie, G. Wang, X. Bao, Advanced Materials, 2019, 0 1902033.
[4] S.R. Foit, I.C. Vinke, L.G.J. deHaart, R.-A. Eichel, Angew. Chem. Int. Ed. 56 (2017) 5402–5411.
[5] T. Ishihara, S. Wang, K.-T. Wu, Solid State Ionics 299 (2017) 60–63.
[6] Y. Zheng, J. Wang, B. Yu, W. Zhang, J. Chen, J. Qiao, J. Zhang, Chem. Soc. Rev. 46 (2017) 1427–1463.
[7] V. Vibhu, J.-M. Bassat, A. Flura, C. Nicollet, J.-C. Grenier, A. Rougier, ECS Transactions 68 (2015) 825–835.
[8] V. Vibhu, A. Flura, C. Nicollet, S. Fourcade, N. Penin, J.-M. Bassat, J.-C. Grenier, A. Rougier, M. Pouchard, Solid State Sci. 81 (2018) 26–31.
[9] V. Vibhu, A. Rougier, C. Nicollet, A. Flura, J.-C. Grenier, J.-M. Bassat, Solid State Ionics 278 (2015) 32–37.
[10] S. Choi, S. Yoo, J. Kim, S. Park, A. Jun, S. Sengodan, J. Kim, J. Shin, H.Y. Jeong, Y. Choi, G. Kim, M. Liu 3 (2013) 2426.
[11] Q. Liu, C. Yang, X. Dong, F. Chen, Int. J. Hydrogen Energy 35 (2010) 10039–10044.
[12] Y. Liu, Y. Cao, S. Yang, D. Yan, B. Chi, J. Pu, L. Jian, Fuel Process. Technol. 135 (2015) 203–206.
[13] K. Zhang, L. Ge, R. Ran, Z. Shao, S. Liu, Acta Mater. 56 (2008) 4876–4889.
[14] F. Chauveau, J. Mougin, J.M. Bassat, F. Mauvy, J.C. Grenier, J. Power Sources 195 (2010) 744–749.
[15] V. Vibhu, A. Rougier, C. Nicollet, A. Flura, S. Fourcade, N. Penin, J.-C. Grenier, J.-M. Bassat, J. Power Sources 317 (2016) 184–193.
[16] E. Boehm, J.M. Bassat, M.C. Steil, P. Dordor, F. Mauvy, J.C. Grenier, Solid State Sci. 5 (2003) 973–981.
[17] C. Ferchaud, J.-C. Grenier, Y. Zhang-Steenwinkel, M.M.A. van Tuel, F.P.F. van Berkel, J.-M. Bassat, J. Power Sources 196 (2011) 1872–1879.
[18] X. Tong, F. Zhou, S. Yang, S. Zhong, M. Wei, Y. Liu, Ceram. Int. 43 (14) (2017) 10927–10933.
[19] A. Aguadero, J.A. Alonso, M.J. Martinez-Lope, M.T. Fernandez-Diaz, M. J. Escudero, L. Daza, J. Mater. Chem. 16 (2006) 3402–3408.
[20] C.N. Munnings, S.J. Skinner, G. Amow, P.S. Whitfield, I.J. Davidson, Solid State Ionics 176 (2005) 1895–1901.
[21] A. Flura, S. Dru, C. Nicollet, V. Vibhu, S. Fourcade, E. Lebraud, A. Rougier, J.-M. Bassat, J.-C. Grenier, J. Solid State Chem. 228 (2015) 189–198.
[22] E. Boehm, J.M. Bassat, P. Dordor, F. Mauvy, J.C. Grenier, P. Stevens, Solid State Ionics 176 (2005) 2717–2725.
[23] V. Vibhu, M.R. Suchomel, N. Penin, F. Weill, J.-C. Grenier, J.-M. Bassat, A. Rougier, Dalton Trans. 48 (2019) 266–277.
[24] R.D. Shannon, Acta Crystallogr. A 32 (1976) 751–767.
[25] V. Vibhu, A. Flura, A. Rougier, C. Nicollet, S. Fourcade, T. Hungria, J.-C. Grenier, J.-M. Bassat, J. Energy Chem. 46 (2020) 62–70.
[26] M.C. Tucker, L. Cheng, L.C. DeJonghe, J. Power Sources 196 (2011) 8313–8322.
[27] V. Vibhu, I.C. Vinke, R.A. Eichel, J.M. Bassat, L.G.J. de Haart, J. Power Sources 444 (2019) 227292.
[28] G. Valderrama, A. Kiennemann, M.R. Goldwasser, Catal. Today 133–135 (2008) 142–148.
[29] J.A. Kilner, C.K.M. Shaw, Solid State Ionics 154–155 (2002) 523–527.
[30] M.C. Biesinger, B.P. Payne, A.P. Grosvenor, L.W.M. Lau, A.R. Gerson, R.S.C. Smart, Appl. Surf. Sci. 257 (2011) 2717–2730.
[31] B.A. Boukamp, A. Rolle, Solid State Ionics 314 (2018) 103–111.
[32] M. Ghamarinia, A. Babaei, C. Zamani, Electrochim. Acta (2020) 136520.
[33] J. Hayd, E. Ivers-Tiffée, J. Electrochem. Soc. 160 (2013) F1197–F1206.
[34] H. Sumi, T. Yamaguchi, K. Hamamoto, T. Suzuki, Y. Fujishiro, J. Power Sources 226 (2013) 354–358.
[35] T.H. Wan, M. Saccoccio, C. Chen, F. Ciucci, Electrochim. Acta 184 (2015) 483–499.

[36] P. Caliandro, A. Nakajo, S. Diethelm, J. Van herle, J. Power Sources 436 (2019) 226838.
[37] S.B. Adler, Solid State Ionics 135 (2000) 603–612.
[38] M.J. Escudero, A. Aguadero, J.A. Alonso, L. Daza, J. Electroanal. Chem. 611 (2007) 107–116.
[39] C. Fu, K. Sun, N. Zhang, X. Chen, D. Zhou, Electrochim. Acta 52 (2007) 4589–4594.
[40] W.G. Bessler, J. Electrochem. Soc. 153 (2006) A1492.
[41] T. Jacobsen, P.V. Hendriksen, S. Koch, Electrochim. Acta 53 (2008) 7500–7508.
[42] A. Flura, C. Nicollet, S. Fourcade, V. Vibhu, A. Rougier, J.M. Bassat, J.C. Grenier, Electrochim. Acta 174 (2015) 1030–1040.
[43] A. Ringuedé, J. Fouletier, Solid State Ionics 139 (2001) 167–177.
[44] E. Siebert, A. Hammouche, M. Kleitz, Electrochim. Acta 40 (1995) 1741–1753.
[45] G.N. Mazo, N.V. Lyskov, L.S. Leonova, Solid State Ionics 182 (2011) 64–70.
[46] J. Wang, F. Meng, T. Xia, Z. Shi, J. Lian, C. Xu, H. Zhao, J.-M. Bassat, J.-C. Grenier, Int. J. Hydrogen Energy 39 (2014) 18392–18404.
[47] N. Grunbaum, L. Dessemond, J. Fouletier, F. Prado, L. Mogni, A. Caneiro, Solid State Ionics 180 (2009) 1448–1452.
[48] F. Mauvy, J.M. Bassat, E. Boehm, J.P. Manaud, P. Dordor, J.C. Grenier, Solid State Ionics 158 (2003) 17–28.
[49] L.-P. Sun, Q. Li, H. Zhao, J.-H. Hao, L.-H. Huo, G. Pang, Z. Shi, S. Feng, Int. J. Hydrogen Energy 37 (2012) 11955–11962.
[50] X. Yu, C. Sui, R. Ren, J. Qiao, W. Sun, Z. Wang, K. Sun, ACS Appl. Energy Mater. 3 (2020) 447–455.
[51] C. Berger, A. Egger, R. Merkle, E. Bucher, B. Stuhlhofer, N. Schrödl, J. Lammer, C. Gspan, G. Logvenov, J. Maier, W. Sitte, J. Electrochem. Soc. 166 (2019) F1088–F1095.
[52] S.B. Adler, Chem. Rev. 104 (2004) 4791–4844.
[53] S.J. Kim, K.J. Kim, A.M. Dayaghi, G.M. Choi, Int. J. Hydrogen Energy 41 (2016) 14498–14506.
[54] Y. Bo, Z. Wenqiang, X. Jingming, C. Jing, Int. J. Hydrogen Energy 33 (2008) 6873–6877.
[55] W. Jiang, Z. Lü, B. Wei, Z.H. Wang, X.B. Zhu, Y.T. Tian, X.Q. Huang, W.H. Su, Fuel Cell. 14 (2014) 76–82.
[56] A. Montenegro-Hernández, J. Vega-Castillo, L. Mogni, A. Caneiro, Int. J. Hydrogen Energy 36 (2011) 15704–15714.
[57] M.A. Laguna-Bercero, H. Monzón, A. Larrea, V.M. Orera, J. Mater. Chem. 4 (2016) 1446–1453.
[58] C. Nicollet, A. Flura, V. Vibhu, A. Rougier, J.-M. Bassat, J.-C. Grenier, Int. J. Hydrogen Energy.
[59] R. Chockalingam, A.K. Ganguli, S. Basu, J. Power Sources 250 (2014) 80–89.
[60] P. Shuk, M. Greenblatt, Solid State Ionics 116 (1999) 217–223.
[61] A. Flura, C. Nicollet, V. Vibhu, A. Rougier, J.-M. Bassat, J.-C. Grenier, Electrochim. Acta 231 (2017) 103–114.